



HAL
open science

Assessment of the Electron Correlation Treatment on the Quantum-Classical Dynamics of Retinal Protonated Schiff Base Models: XMS-CASPT2, RMS-CASPT2, and REKS Methods

Leonardo Barneschi, Danil Kaliakin, Miquel Huix-Rotllant, Nicolas Ferré,
Massimo Olivucci

► To cite this version:

Leonardo Barneschi, Danil Kaliakin, Miquel Huix-Rotllant, Nicolas Ferré, Massimo Olivucci. Assessment of the Electron Correlation Treatment on the Quantum-Classical Dynamics of Retinal Protonated Schiff Base Models: XMS-CASPT2, RMS-CASPT2, and REKS Methods. *Journal of Chemical Theory and Computation*, 2023, 19 (22), pp.8189-8200. 10.1021/acs.jctc.3c00879 . hal-04291568

HAL Id: hal-04291568

<https://hal.science/hal-04291568>

Submitted on 16 Feb 2024

HAL is a multi-disciplinary open access archive for the deposit and dissemination of scientific research documents, whether they are published or not. The documents may come from teaching and research institutions in France or abroad, or from public or private research centers.

L'archive ouverte pluridisciplinaire **HAL**, est destinée au dépôt et à la diffusion de documents scientifiques de niveau recherche, publiés ou non, émanant des établissements d'enseignement et de recherche français ou étrangers, des laboratoires publics ou privés.

1 Assessment of the electron correlation treatment on the quantum-
2 classical dynamics of retinal protonated Schiff base models: XMS-
3 CASPT2, RMS-CASPT2 and REKS methods.

4
5 Leonardo Barneschi¹, Danil Kaliakin^{2,*}, Miquel Huix-Rotllant,³ Nicolas Ferré,³ Michael
6 Filatov(Gulak)⁴ and Massimo Olivucci^{1,2,*}

7
8 ¹Dipartimento di Biotecnologie, Chimica e Farmacia, Università di Siena, I-53100, Siena, Italy.

9 ²Department of Chemistry, Bowling Green State University, Bowling Green, OH, 43403, USA.

10 ³Aix-Marseille Université, CNRS, Institut Chimie Radicale, 13013 Marseille, France.

11 ⁴Department of Chemistry, Southern Methodist University, Dallas, TX, 75275, USA.

12
13 Corr. Authors e-mail:

14 * Danil Kaliakin, dskalyakin@outlook.com

15 * Massimo Olivucci, olivucci@unisi.it

16
17 **Abstract**

18
19 We compare the performance of three different multiconfigurational wavefunction-based
20 electronic structure methods and two implementations of the spin-restricted ensemble-referenced
21 Kohn-Sham (REKS) method. The study is characterized by three features: i) it uses a small set of
22 quantum-classical trajectories rather than potential energy surface mapping, ii) it focuses,
23 exclusively, on the photoisomerization of retinal protonated Schiff base models, iii) it probes the
24 effect of both methyl substitution and the increase in length of the conjugate π -system. For each
25 tested method, the corresponding analytical gradients are used to drive the quantum-classical
26 (Tully's FSSH method) trajectory propagation including the recent multistate XMS-CASPT2 and
27 RMS-CASPT2 gradients. It is shown that while CASSCF, XMS-CASPT2 and RMS-CASPT2
28 yield consistent photoisomerization dynamics descriptions, REKS produces, in some of these
29 systems, a qualitatively different behavior that is attributed to a flatter and topographically
30 different excited state potential energy surface. The origin of this behavior is traced back to the
31 effect of the employed density functional approximation. The above studies are further expanded
32 by benchmarking, at the CASSCF and REKS levels, the electronic structure methods using a
33 QM/MM model of the visual pigment rhodopsin.

I. INTRODUCTION

The penta-2,4-dieniminium cation (PSB3), a protonated imine featuring three conjugated double-bonds, is a computationally inexpensive model of the retinal chromophore (rPSB) of rhodopsins.¹⁻⁴ (see Fig. 1A, top) In rPSB a cationic nitrogen polarizes the conjugated framework leading to changes in electronic character upon electronic excitation and geometrical deformation.⁵ These changes are qualitatively replicated by PSB3 where excitation from the ground state (S_0) to the first singlet electronically excited state (S_1) triggers a charge-transfer (CT) from the -C1=N to the C5=C4- moiety. Such character then changes in magnitude along the S_1 -C2=C3- isomerization path that ends at a S_1/S_0 conical intersection (CoIn) to continue, after decay, along reactive and unreactive S_0 relaxation paths.^{1,6-8} Despite the different characteristics of the photoisomerization process shared by PSB3 and rPSB, the increased conjugation in the longer rPSB skeleton produces a longer excited state lifetime. Nonetheless, since the present manuscript is focused on qualitative rather than quantitative features and how these are captured by different electronic structure methods, PSB3 is assumed to be a suitable model. In fact, PSB3 has been systematically used in the past to benchmark other changes associated with the use of different electronic structure methods.⁹⁻¹¹ These and other properties make PSB3 an ideal candidate for benchmarking electronic structure methods that are required to deal with extended potential energy regions with strong electron correlation effects of both S_0 and S_1 states.^{6,12}

Past benchmark projects^{8-10,13-24} have focused almost exclusively on the mapping of the potential energy surfaces (PESs) of parent PSB3. Yet, rPSB features six conjugated double-bonds as well as different methyl substitutions and its mechanism is presently studied using quantum-classical trajectories⁵ beyond the Born-Oppenheimer approximation rather than PES cross-sections or minimum energy paths. Therefore, in the present contribution we study the effect of the incorporation in PSB3 of one methyl substituent and π -system length increase on both relaxed S_1 PES cross-sections and quantum-classical trajectory calculations. The computational details of quantum-classical nonadiabatic molecular dynamics simulations used in present study are described in the METHODS section. Our main target is to describe how selected multistate wavefunction and density functional based electronic structure methods describe such properties at both the static and quantum-classical dynamic levels.

The analysis of the trajectories will focus on two PSB3 key geometrical parameters (see Fig. 1B, bottom): (i) the torsional angle α describing the -C2=C3- isomerization coordinate in

67 terms of the C4-C3-C2-C1 dihedral angle, and (ii) the bond length alternation (BLA) describing
68 the degree of π -electron delocalization. The BLA is computed in terms of the difference between
69 the average length of the formal single-bonds and the formal double-bonds along conjugated
70 polyene chain of the investigated protonated Schiff base derivatives, as defined in their closed-
71 shell electronic ground state. As schematically displayed in Fig. 1C, BLA and α will be used to
72 rationalize the changes seen in the computed quantum-classical trajectories. Quantum-classical
73 trajectories typically start with a kick (i.e. vertical) excitation to the S_1 state with some random
74 initial velocity on the Franck-Condon (FC) region, propagate along the S_1 PES and, after hopping
75 to S_0 in the region of a CoIn seam (i.e. S_1/S_0 intersection space) where α is ca. 90° , relax on the S_0
76 PES either generating an isomer (reactive red population) or returning to its original configuration
77 (unreactive blue population).²⁵ Accordingly, for each model considered (see below), we compute
78 an S_1 relaxed scan along α as well a set of 50 quantum-classical trajectories (see Fig. 1B). The
79 results are then presented in terms of values of static (S_1 energy barrier ($E^a_{S_1}$), S_1 - S_0 energy gap at
80 $\alpha = 90^\circ$ ($E^{90}_{S_1-S_0}$)) and dynamic (BLA before and after S_1 relaxation ($BLA_{S_0-S_1}$), S_1 lifetime (τ_{S_1})
81 and isomerization quantum efficiency (QY^{iso})) descriptors. See the legend of Table 1 for the
82 definition of these quantities. We must stress that being only based on a small number of
83 trajectories, “statistical” descriptors such as $BLA_{S_0-S_1}$, τ_{S_1} and, most importantly, QY^{iso} , are only
84 indicative.

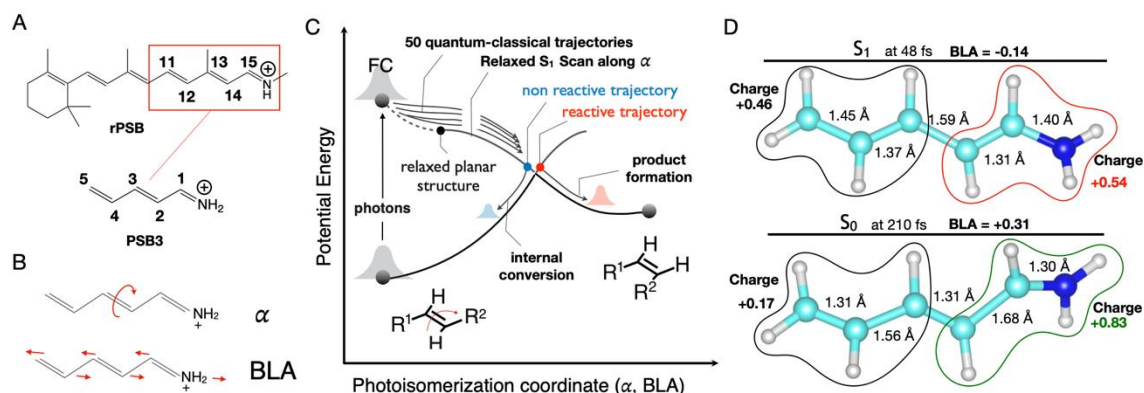
85 Previous work on PSB3⁷ has shown that large positive BLA values indicate a covalent
86 (COV) character where the cationic charge is located near the -C1=N moiety, while near-zero or
87 even negative values inform on the percentage of charge transfer (CT) character associated with
88 the cationic charge delocalization towards the C5=C4- moiety (see Fig. 1D). As we will further
89 detail below, such a relationship between geometry and electronic character can be used as a
90 descriptor of the impact of the treatment of electron correlation in each studied electronic structure
91 method on both PES topography and progression along quantum-classical trajectories.

92 Taking PSB3 and CASSCF as the reference rPSB model and electronic structure method
93 respectively, the changes in the descriptor values, document the effect of: (i) methyl substitution
94 and increase in number of conjugated double bonds in the 1-methyl-*cis*-PSB3 (1cMePSB3), 4-
95 methyl-*cis*-PSB3 (4cMePSB3), 4-methyl-*trans*-PSB3 (4tMePSB3), and hepta-2,4,6-trieniminium
96 cation (PSB4) models (see Fig. 2A) and (ii) the change from CASSCF to XMS-CASPT2, RMS-
97 CASPT2, and REKS’s SSR(2,2) and SSR(3,2) flavors. The XMS-CASPT2, RMS-CASPT2 levels

98 (collectively called CASPT2-levels) represent multistate wavefunction methods where CASSCF
 99 provides the zeroth-order multiconfigurational wavefunction used for successive second-order
 100 perturbation theory corrections.^{26–28} Instead, SSR(2,2) and SSR(3,2) correspond to two different
 101 multistate implementations (REKS-levels) of spin-restricted ensemble-referenced Kohn-Sham
 102 density functional theory.^{29–31} Notice that, in all cases, the calculations necessary to determine the
 103 descriptors are performed by using the corresponding analytical gradients. Indeed, the present
 104 work has been partially prompted by the fact that XMS-CASPT2 and RMS-CASPT2 gradients
 105 have been made available in OpenMolcas,²⁷ and by the in-house development of an interface
 106 between OpenMolcas and GAMESS-US^{32–34} providing REKS gradients. Previous PES studies on
 107 PSB3 compared the performance of SSR(2,2) and CASSCF^{13,18,20} as well as for SSR(2,2) and
 108 XMS-CASPT2²¹. However, no comparison of the performance of SSR(2,2) vs. SSR(3,2) and
 109 RMS-CASPT2 and no description of the changes induced by PSB3 modification have been
 110 reported.

111 While CASSCF misses a large part of the electron correlation energy, CASSCF-based
 112 quantum mechanics/molecular mechanics (QM/MM) models of rPSB embedded in the cavity of
 113 the visual pigment rhodopsin (Rh), have been used in several quantum-classical trajectory
 114 studies.^{5,25,35–37} Remarkably, such studies have shown that such models reproduce, among other
 115 observables, the experimentally observed τ_{S1} and QY^{iso} . Here, we benchmark, for the first time,
 116 the same type of QM/MM model after replacing CASSCF with SSR(2,2) and compare some of
 117 the obtained descriptors with the experimental data.

118



119

120 **Fig. 1.** Structure and reactivity of PSB3. (A) Comparison between the all-*trans* rPSB structure and the PSB3
 121 structure. The framed moiety informs on the similarity of the two structures. (B) Most relevant geometrical
 122 parameters in this work. (C) Schematic representation of the S_1 and S_0 potential energy profiles along the

123 trans to cis -C2=C3- isomerization path of PSB3. A set of quantum-classical trajectories, together with a
124 reactive (red circle at the hop point) and one non-reactive (blue circle at the hop point) trajectory, are also
125 displayed. Note that the S_1 isomerization path discussed in this paper connects a S_1 relaxed planar structure
126 to the CoIn and it is obtained by scanning the S_1 PES along α . (D) Relationship between BLA values and
127 charge distribution in PSB3 along a representative CASSCF-driven quantum-classical trajectory. Top: an
128 S_1 PSB3 structure extracted before decay to S_0 . Bottom: the same structure after decay (surface hop) to S_0 .
129 The charges on the two circled moieties of PSB3 are computed as sums of the Mulliken charges of the
130 atoms of the corresponding moieties. These are $R^1 = \text{H}_2\text{C}=\text{CH}-\text{CH}$ and $R^2 = \text{CH}-\text{CH}=\text{NH}_2$. It can be seen
131 how a negative BLA is associated with a ca. 50% charge transfer while a positive BLA with a minor ca.
132 20% charge transfer.

133

134 As anticipated above, past studies of PSB3 focused on the shape of PESs and CoIn
135 properties. These studies showed that the treatment of electron correlation in various electronic
136 structure methods (see the Supporting Information for a list of acronyms) such as TDDFT,^{13,18,19}
137 SF-TDDFT,¹³ EOM-SF-CCSD(dT),^{8,13} CASSCF,^{8,10,13,14,18–24,38}
138 MRCISD,^{8,10,23} MRCISD+Q,^{8,10,18,23} QD-NEVPT2,^{10,13} CC2,^{9,19,22} ADC,⁹ SS-
139 CASPT2,^{10,13,14,19,22–24} MS-CASPT2,^{10,14,21,23,24} XMS-CASPT2,^{14,21,23} XMCQDPT2,^{10,13} and
140 REKS^{13,18,20,21} impacts the isomerization coordinate and energy profile. However, fewer studies
141 addressed the effect of such methods on quantum-classical trajectories.^{13,15–17} Among others,
142 Zhang and Herbert compared SF-TDDFT and LR-TDDFT quantum-classical trajectories;¹⁵
143 Filatov et al. discussed the outcomes of quantum-classical trajectories driven by REKS and MS-
144 CASPT2;¹⁶ Gozem et al. compared quantum-classical trajectories generated using SS-CASPT2
145 and CASSCF;¹³ Instead, Liu et al. reported on the comparison for MS-CASPT2 and CASSCF.¹⁷

146 Due to the missing dynamic electron correlation treatment, CASSCF does not correctly
147 reproduce vertical excitation energies (VEEs) and, consequently the S_1 and S_0 energy profiles.^{39–}

148 ⁴¹ An improved description can be obtained after multiconfigurational perturbative correction
149 using, for instance, single state (SS-CASPT2) or, multi-state (MS-CASPT2) perturbative methods.
150 However, MS-CASPT2 leads to unphysical predictions in the intersection space region^{13,28,42} that
151 can be improved using the extended multi-state XMS-CASPT2 method.²⁶ In fact, Schapiro and
152 coworkers demonstrated that, for PSB3, XMS-CASPT2 overcomes such issue.²³ In particular, the
153 latest variant of it, called “rotated multistate CASPT2” (RMS-CASPT2), is the least sensitive to

154 the number of states included in calculations and can potentially offer certain accuracy
155 improvements,²⁷ even if extensive benchmarking has not been reported.

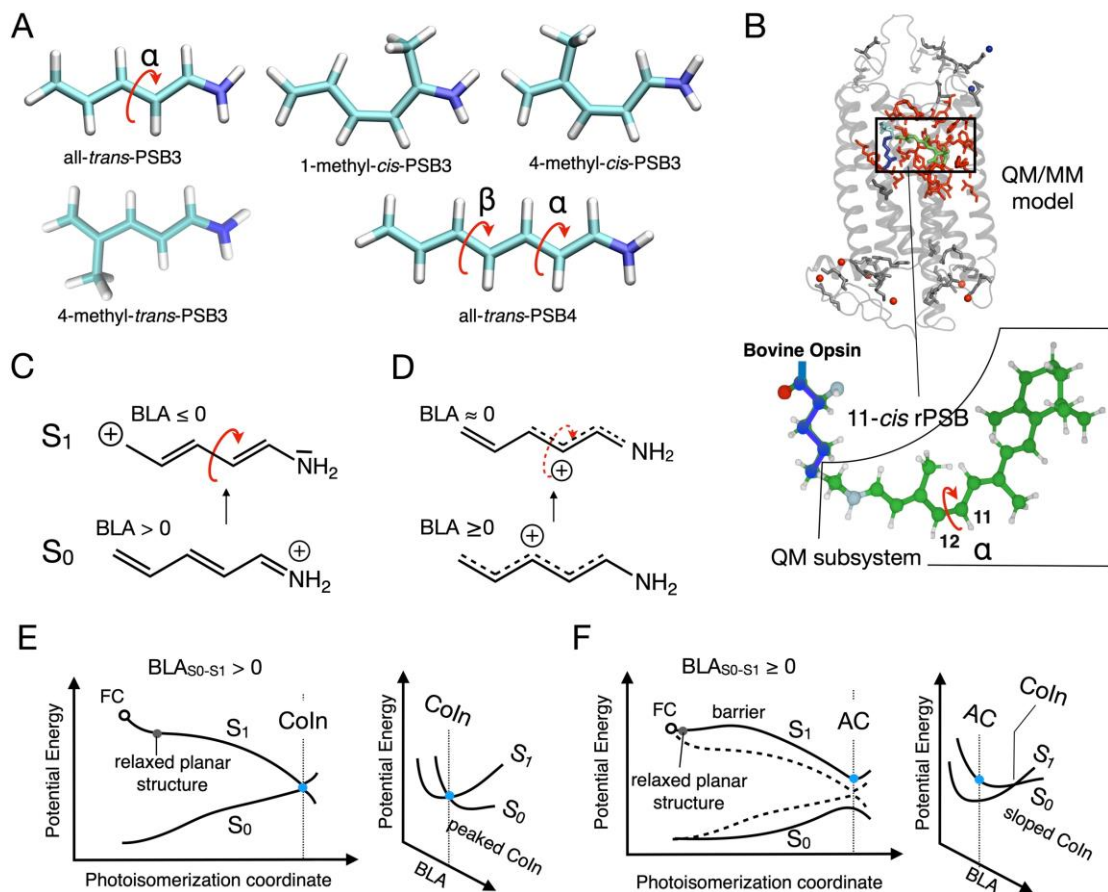
156 The spin-restricted ensemble-referenced Kohn-Sham (REKS) method is a state-averaged
157 extension (SA-REKS), and the state-interaction state-averaged REKS (SI-SA-REKS or, for short,
158 SSR) employ ensemble-density functional theory (eDFT)⁴³ to introduce non-dynamic electron
159 correlation into the description of S_0 and S_1 states and produces VEEs in a way similar to a
160 wavefunction-based multi-state multi-configurational method.^{29,44,45} In fact, eDFT enables a
161 seamless incorporation of multiconfigurational effects, where the results of standard Kohn-Sham
162 (KS) computations are recovered for weakly correlated (e.g. single-reference) systems. In this way,
163 the study of photochemical and thermal reactivities of medium-size organic molecules (e.g. 40-50
164 carbon atoms with 14-16 delocalized electrons) becomes treatable and can be used to simulate
165 reactive dynamics.⁴⁶ Accordingly, we include in our benchmark study SSR(2,2) and SSR(3,2)
166 methods, where SSR(2,2) employs the perfectly spin-paired singlet (PPS) and the open-shell
167 singlet (OSS) configurations, while the configuration space of SSR(3,2) method is augmented in
168 addition by the doubly excited singlet (DES) configuration thus offering, in principle, a description
169 of doubly excited state character and the S_2 state. In the present study, REKS calculations are done
170 with BHHLYP functional,⁴⁷⁻⁴⁹ however, other functionals are tested as well.

171 As anticipated above, the interpretation of our results will be guided by a qualitative
172 theoretical framework based on $BLA_{S_0-S_1}$ values.^{7,50} More precisely:

173 i) Positive $BLA_{S_0-S_1}$ values (i.e. a large decrease of the BLA value upon S_1 relaxation)
174 would indicate large CT character in S_1 (Fig. 2C) and a limited charge delocalization in S_0 . A
175 $BLA_{S_0-S_1}$ approaching zero (i.e. a small change in BLA upon S_1 relaxation) would instead indicate
176 substantial mixing of COV and CT characters and an increased S_1 and S_0 charge delocalization
177 (Fig. 2D),

178 ii) Large CT character increasing along the isomerization path (trajectory) would lead to a
179 barrierless (fast) isomerization and a topographically peaked CoIn (Fig. 2E). In contrast, a mixed
180 COV and CT character that also increases in COV weight along the S_1 isomerization path
181 (trajectory) would lead to a barrier controlled (slow or blocked) isomerization and topographically
182 sloped CoIn that manifest itself through the presence of an avoided crossing (AC) located along
183 the path (Fig. 2F).

184



185
 186 **Fig. 2.** rPSB models employed in this work. (A) S_0 structures of PSB3, its methylated derivatives and PSB4.
 187 (B) Structure of the QM/MM model of Rh used in the present study. The 11-*cis* rPSB structure corresponds
 188 to the QM subsystem treated at the QM level. The rest of the model is treated at the MM level and comprises
 189 the parts in blue, red and the ribbons (MM subsystem). The MM residues in red, in blue and the QM
 190 subsystem are free to relax during the quantum-classical trajectory calculations. (C) The qualitative
 191 relationship between BLA value and electronic structure for a S_0 dominated by a COV character. (D) The
 192 same relationship for a S_0 dominated by a mixed COV/CT character. (E) Expected S_1 energy profiles when
 193 S_1 is dominated by a CT character (and S_0 dominated by a COV character). The diagram on the right
 194 displays the energy profiles along a BLA cross section intercepting the CoIn. (F) The same energy profiles
 195 when S_1 is dominated by a mixed COV/CT character (and S_0 also dominated by a mixed e COV/CT
 196 character). The dashed curves display the energy profiles of panel E, for comparison. The diagram on the
 197 right displays the BLA cross section at the avoided crossing (AC) region.
 198

199 **II. RESULTS AND DISCUSSION**

200

201 The results are presented in three subsections focused on PSB3 and derivatives, PSB4 and
 202 the QM/MM Rh model, respectively. The first two subsections start with a description of the
 203 changes due to PSB3 structure modifications and (mainly) looking at the CASSCF results. This is
 204 followed by a discussion of the differences between the CASPT2-levels and REKS-levels. We will
 205 not look at quantitative differences but focus as much as possible on qualitative (mechanistic)
 206 differences. In the first section of the Supporting Information and Table S1, we show that, despite
 207 the limited number of trajectories propagated for each method, this statistic is in fact sufficient to
 208 deliver the key differences between the methods. Fig. S1 shows excited state lifetime ($\tau_{S_1\text{-fit}}$) from
 209 exponential fitting of the S_1 population fraction decay. However, in the main text, we will reference
 210 to excited state lifetimes, τ_{S_1} , calculated as the simple average time of the S_1 -to- S_0 decay events.
 211 The full set of calculated descriptor values are collected in Table 1.

212

213 **Table 1.** Values of static and dynamic descriptors (see text). $BLA_{S_0-S_1}$ is defined as the BLA time
 214 average between 0 and 50 fs (representing the initial S_1 relaxation) minus the average BLA value
 215 at 0 fs, BLA_{S_0} (in brackets). $E^a_{S_1}$ represents the energy difference between the initial (i.e. relaxed
 216 planar structure in Fig. 1C) point and the highest point found along the S_1 isomerization (α) energy
 217 profile. $E^{CI}_{S_1-S_0}$ is the S_1 - S_0 energy gap in conical intersection region. FTND represents the fraction
 218 of trajectories that remains in the S_1 state at the end of the simulation. τ_{S_1} corresponds to the
 219 average S_1 -to- S_0 hop time. QY^{iso} is computed in terms of the fraction of hops leading to an
 220 isomerized product. The trajectories contributing to FTND are not considered in the QY^{iso}
 221 calculation. The values in parenthesis refer to the fraction of trajectories following the
 222 corresponding path. QY^{iso} standard deviations are also reported as ΔQY^{iso} .

223

	$BLA_{S_0-S_1}$ (Å)	$E^a_{S_1}$ (kcal/mol)	$E^{90}_{S_1-S_0}$ (kcal/mol)	FTND	τ_{S_1} (fs)	QY^{iso}	ΔQY^{iso}
PSB3	$BLA_{S_0-S_1}, BLA_{S_0}$						
CASSCF	0.14 (0.085)	0.0	1.4	0.00	109	0.63	0.068
XMS-CASPT2	0.10 (0.076)	0.0	1.7	0.06	107	0.66	0.067
RMS-CASPT2	0.07 (0.075)	0.0	0.8	0.04	129	0.60	0.069
SSR(2,2)	0.09 (0.077)	0.4	8.6	0.04	159	0.64	0.068

SSR(3,2)	0.09 (0.077)	0.0	8.6	0.00	155	0.70	0.065
1cisMePSB3							
CASSCF	0.15 (0.100)	0.0	0.0	0.00	105	0.62	0.069
XMS-CASPT2	0.09 (0.091)	0.0	0.6	0.00	114	0.56	0.070
RMS-CASPT2	0.06 (0.083)	0.0	1.1	0.02	164	0.61	0.069
SSR(2,2)	0.09 (0.087)	0.0	4.1	0.00	126	0.55	0.070
SSR(3,2)	0.10 (0.087)	0.0	4.2	0.00	108	0.39	0.069
4cisMePSB3							
CASSCF	0.09 (0.089)	0.0	1.3	0.00	132	0.59	0.070
XMS-CASPT2	0.05 (0.085)	0.0	2.8	0.14	>142	0.67	0.066
RMS-CASPT2	0.04 (0.077)	0.0	0.3	0.04	179	0.63	0.068
SSR(2,2)	0.04 (0.076)	0.0	11.3	0.00	191	0.62	0.069
SSR(3,2)	0.04 (0.076)	0.0	11.3	0.04	184	0.48	0.071
4transMePSB3							
CASSCF	0.11 (0.087)	0.0	2.0	0.04	148	0.60	0.069
XMS-CASPT2	0.04 (0.083)	0.0	2.8	0.40	>166	0.48	0.071
RMS-CASPT2	0.04 (0.076)	0.0	0.3	0.38	>240	0.66	0.067
SSR(2,2)	0.03 (0.065)	0.5	10.5	0.05	227	0.60	0.069
SSR(3,2)	0.05 (0.064)	0.3	12.3	0.12	>217	0.51	0.071
PSB4 a, b and c indicate isomerization along differed double bonds)		a. C2=C3 b. C4=C5	a. C2=C3 b. C4=C5		a. C2=C3 b. C4=C5	a. C2=C3 b. C4=C5 c. C6=C7	a. C2=C3 b. C4=C5 c. C6=C7
CASSCF	0.12 (0.080)	0.0, ^a 0.1 ^b	2.8, ^a 0.7 ^b	0.00	228, ^a - ^b	0.58 (0.92), ^a - (0.04) ^b , - (0.04) ^c	0.070 ^a
XMS-CASPT2	0.07 (0.067)	0.0, ^a 0.1 ^b	10.6, ^a 4.5 ^b	0.00	306, ^a - ^b	0.54 (0.86), ^a - (0.07) ^b , - (0.08) ^c	0.070 ^a
RMS-CASPT2	0.05 (0.061)	0.0, ^a 0.3 ^b	8.0, ^a 6.9 ^b	0.16	>370, ^a - ^b	0.60 (0.70), ^a 0.00 ^b , - (0.14) ^c	0.069 ^a
SSR(2,2)	0.05 (0.059)	1.3, ^a 0.3 ^b	19.8, ^a 1.4 ^b	0.64	-, ^a >349 b	- , - ^a 0.75 (0.16) ^b , - (0.02) ^c	0.061 ^b
SSR(3,2)	0.06 (0.063)	0.9, ^a 0.0 ^b	19.8, ^a 1.4 ^b	0.54	-, ^a >261 b	- , - ^a 0.58 (0.24) ^b , - (0.04) ^c	0.070 ^b
Rh							
CASSCF	0.12 (0.106)	-	-	0.03	97	0.64	0.068
SSR(2,2)	0.06 (0.073)	-	-	0.30	>179	0.21	0.058

224

225

From PSB3 to methyl-substituted PSB3

226

When comparing PSB3 to 4cMePSB3 and 4tMePSB3, all electronic structure methods

227

show a decrease in $BLA_{S_1-S_0}$ (e.g. from 0.14 to 0.09-0.11 Å for CASSCF and the CASPT2-levels

228

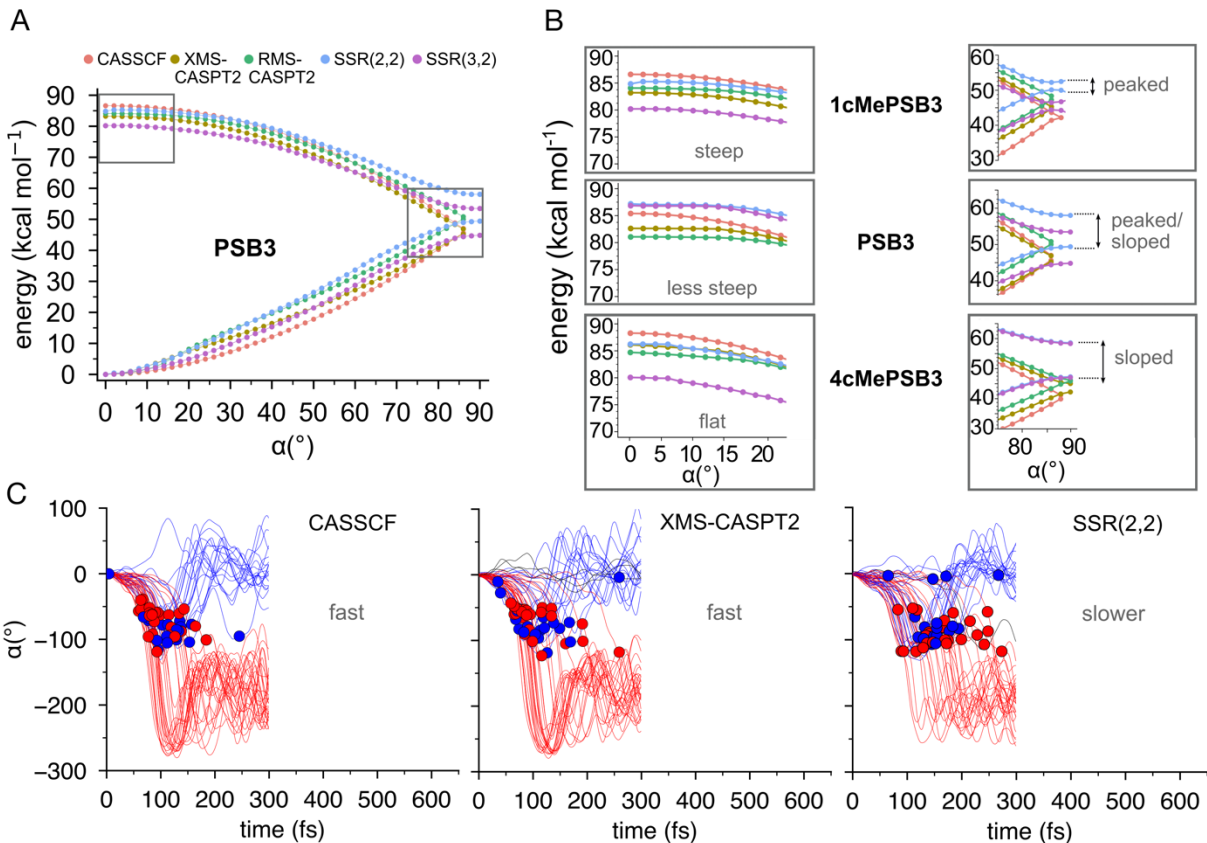
and from 0.09 to 0.03-0.04 Å for SSR(2,2)) pointing to a change of the S_1 and S_0 electronic

229 structure upon Me-substitution at C4. This is explained by the Me hyperconjugation stabilizing the
230 positive charge on the C5-C4-C3- moiety and, thus, increasing the weight of the CT character in
231 S_0 and, consequently, the weight of COV character in S_1 (compare Fig. 2C and 2D) with respect
232 to PSB3. This yields more mixed CT/COV characters in both states. Me-substitution at C1 in
233 1cMePSB3 does not show such a mixing effect as the hyperconjugation further stabilizes the COV
234 character in S_0 (and, in principle, the CT character in S_1). The slight decrease in $BLA_{S_1-S_0}$ value
235 observed in some cases (e.g. from 0.10 to 0.09 Å at the XMS-CASPT2 level) in 1cMePSB3 with
236 respect to PSB3 is thus attributed to a compensatory effect of the steric repulsion (Fig. S2) between
237 the Me substituent and the CH group in C4. Such steric effect is also present in 4cMePSB3
238 (between Me at C4 and the CH group at C1) but absent in 4tMePSB3.

239 The comparison of the initial part of the PSB3 and 4cMePSB3 and 4tMePSB3 S_1
240 isomerization energy profiles (see Fig. 3A and Fig. 3B) along the -C2=C3- isomerization
241 coordinate (α) display a transition to a slightly reduced slope (4tMePSB3 shows a flatter profile
242 due to a reduced steric repulsion between Me substituent and the CH group at C1) and, for the
243 REKS-levels, a change in the CoIn topography as indicated by the increased S_1-S_0 energy gap. The
244 above characterization is confirmed by the trajectory calculations that show a 20-40 fs increase in
245 τ_{S_1} at the CASSCF level for 4cMePSB3 and 4tMePSB3 with respect to PSB3 (Table 1). In contrast,
246 1cMePSB3 does not show a significant change in τ_{S_1} (Fig. 3C). The complete isomerization energy
247 profiles along the -C2=C3- isomerization coordinate (α) in 1cMePSB3, 4cMePSB3, and
248 4tMePSB3 are shown in Fig. S3.

249 With the only exception of SSR(3,2) and despite the above changes, the estimated QY^{iso}
250 does not show substantial variations upon Me-substitution. It is possible that the additional
251 configuration in SSR(3,2) alters the phase relationship between the critical modes determining the
252 QY^{iso} value.³⁶ This hypothesis remains to be investigated.

253



254
 255 **Fig. 3.** PSB3 S_1 and S_0 energy profiles along the relaxed S_1 PES scan driven by α and related quantum-
 256 classical trajectories. (A) S_1 and S_0 energy profiles along the PSB3 scan from an S_1 relaxed planar structure
 257 to a $\alpha = 90^\circ$ twisted structure. The FC and CoIn regions (left and right framed regions, respectively) are
 258 detailed in panel B. (B) Left. FC region of the S_1 energy profile. Right. CoIn region of the S_1 energy profile.
 259 The color code is the same as the one in panel A. (C) Progression of α along three different sets of PSB3
 260 quantum-classical trajectories computed with three different levels of electronic structure theory. Blue
 261 circles correspond to S_1 -to- S_0 surface hops leading back to the reactant (unreactive) while red circles
 262 correspond to hops leading to the photoproduct (reactive).

263
 264 **CASPT2-levels.** In PSB3, the $BLA_{S_1-S_0}$ values produced by the XMS-CASPT2, RMS-
 265 CASPT2 are reduced (0.10 Å and 0.07 Å for XMS-CASPT2 and RMS-CASPT2, respectively)
 266 and with respect to CASSCF (0.14 Å), implicating that the recovery of the dynamic electron
 267 correlation leads to a slightly flatter S_1 energy profile confirmed by, for instance, a 20 fs increase
 268 of τ_{S_1} at the RMS-CASPT2 level (compare left and central panels in Fig. 3C) with respect to
 269 CASSCF. Indeed, when comparing PSB3 to 4cMePSB3 and 4tMePSB3 that have augmented S_1
 270 COV characters, one sees a large $BLA_{S_1-S_0}$ variation ultimately leading to values as small as 0.03-

271 0.05. This implies even flatter S_1 energy profiles justifying the >30 fs increase in τ_{S_1} with respect
272 to PSB3. Notice that at the XMS-CASPT2 level the S_1 progression becomes, for 10-40% of the
273 trajectories (see FTND value in Table 1 for 4cMePSB3 and 4tMePSB3), slow enough to prevent
274 decay to S_0 within the simulation time. Again, despite such τ_{S_1} variations, there is no qualitative
275 change in QY^{iso} that remains close to the CASSCF value. The trajectories calculated with all CAS-
276 level methods for PSB3 and substituted PSB3 models are shown in Fig. S4 and Fig. S5.

277 **REKS-levels.** For PSB3, SSR(2,2) and SSR(3,2) replicate the behavior of the CASPT2-
278 levels except for the change in topography of the CoIn that now appears strongly sloped (i.e. it
279 shows an AC) as the ca. 10 kcal/mol values of $E^{90}_{S_1-S_0}$ indicate. Things do not change much when
280 comparing PSB3 to 4cMePSB3 or 4tMePSB3 but a change is observed in 1cMePSB3 that displays
281 substantially reduced S_1/S_0 gap at 90° . In fact, when compared to CASSCF, PSB3 displays similar
282 $BLA_{S_1-S_0}$ variations induced by Me-substituent and a similar ca. 30 fs increase in τ_{S_1} (compare
283 central panel and right panel in Fig. 3C). The QY^{iso} computed at the SSR(2,2) level remains close
284 to the CASSCF value but significantly decreases when SSR(3,2) is used. The trajectories
285 calculated with SSR(2,2) and SSR(3,2) for PSB3 and substituted PSB3 models are shown in Fig.
286 S6 and Fig. S7.

287 We conclude that, in general, the dynamics of PSB3 studied at the CASSCF, CASPT2-
288 levels and REKS-levels yields the same qualitative mechanisms, timescales and QY^{iso} 's (with the
289 only exception of the SSR(3,2) level). In fact, when comparing PSB3 with 4cMePSB3 or
290 4tMePSB3, all levels show an increase in the S_1 COV character along the S_1 isomerization
291 coordinate and longer τ_{S_1} . It is also evident that the S_1 COV character also increases when passing
292 from CASSCF to the perturbatively corrected CASPT2-levels and, most notably, to the REKS-
293 levels, but this does not seem to have a qualitatively important impact on the resulting
294 isomerization dynamics in the PSB3 derivatives where the extension of the π -system is limited.

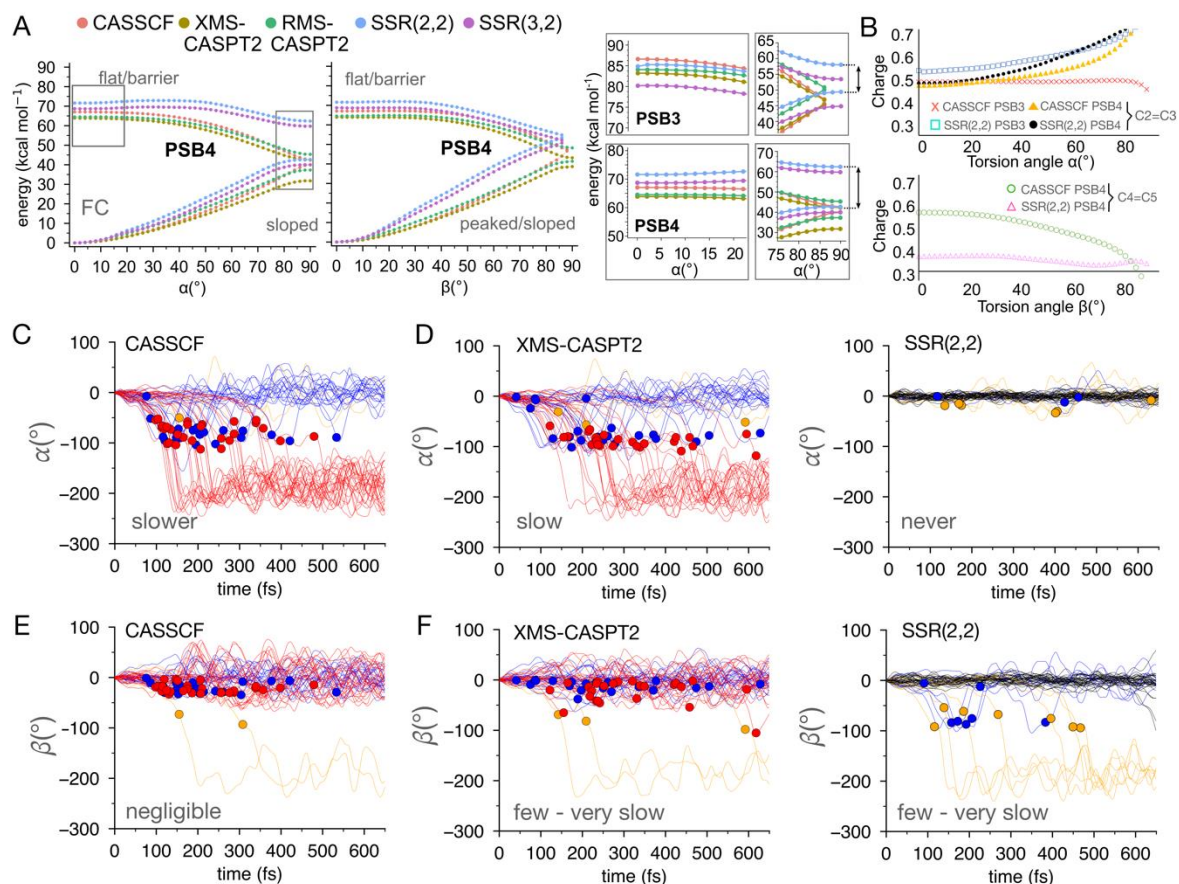
295

296 **From PSB3 to PSB4**

297 The CASSCF data shows a 0.14 to 0.12 decrease in $BLA_{S_1-S_0}$ when moving from PSB3 to
298 PSB4 pointing to a reduced electronic structure change towards a more mixed S_1 electronic
299 structure. In fact, in PSB3 we see, upon S_1 relaxation, a ca. 0.1 charge translocation (see Fig. 4B,
300 top) from the C2-C1-N to the C5-C4-C3 moiety. In PSB4 this translocation is reduced to 0.03 that
301 is, as discussed above, consistent with the decrease in $BLA_{S_1-S_0}$ and increase in COV character

302 with respect to PSB3. This change is, as expected (according to Scheme 2F), consistent with the
303 slope change in the initial part of the S_1 energy profile along the -C2=C3- isomerization coordinate
304 (α) displayed in Fig. 4A. There is, however, another observation relative to the charge
305 translocation. While in PSB3 its magnitude does not change until nearby a CoIn region is entered
306 at ca. 75° twisting and then goes towards larger CT weights, in PSB4 the charge translocation starts
307 to revert around 40° twisting and continue to decrease until the CoIn region is reached, indicating
308 that, after the initial progression, the COV weight in S_1 is increases, not decreases, along the S_1
309 isomerization coordinate. This leads to the flatter PSB4 energy profile along α with respect to
310 PSB3 (compare the “PSB3” panel of Fig. 3B with the left panel of Fig. 4A) and, consequently, to
311 a 120 fs increase in τ_{S_1} as well as by a more than 200 fs increase (from 150 fs to ca. 350 fs) in the
312 decay time-range (compare Fig. 4C with Fig. 3C) at the CASSCF level. On the other hand, the -
313 C2=C3- isomerization of PSB4 described by α , has a QY^{iso} of 0.58 and its therefore only slightly
314 reduced with respect to that of PSB3.

315
316 The alternative progression (see Fig. 4A center) along the -C4=C5- isomerization
317 coordinate (β) shows a charge translocation (see Fig. 4B, bottom) corresponding to a constant CT
318 character increase rather than decrease. However, the -C4=C5- channel is found to be energetically
319 less favorable as only two trajectories decay along that path and, therefore, t_{S_1} and QY^{iso} remain
320 undefined even as qualitative descriptor. As shown in Figure S12, this behavior is attributed to the
321 energy barrier (or increased flatness) existing along the β coordinate with respect to the α
322 coordinate.



323
 324 **Fig. 4.** PSB4 S_1 and S_0 energy profiles along the relaxed S_1 PES scan and quantum-classical trajectories
 325 driven by α and β (C2=C3 and C4=C5 respectively. See Fig. 2A). (A) S_1 and S_0 energy profiles along the
 326 coordinates corresponding to twists around α and β . The inset on the right correspond to the framed FC and
 327 CoIn regions seen in the left panel. B. Progression of the CT computed as the value of the positive charge
 328 residing on the N-containing moieties C2-C1-N and C4-C3-C2-C1-N for the scan along α (PSB3 and PSB4)
 329 and β (PSB4) respectively. (C) Propagation of α along the simulated CASSCF-driven PSB4 trajectories.
 330 Red lines and red circles correspond to trajectories that undergo C2=C3 isomerization and their hopping
 331 points, respectively. Orange lines and orange circles correspond to trajectories that undergo C4=C5
 332 isomerization and their hopping points, respectively. Blue lines and blue circles correspond to unproductive
 333 trajectories and their hopping points, respectively. Black lines correspond to trajectories that did not
 334 undergo surface hop. (D) Same as C for XMS-CASPT2 (left panel) and SRR(2,2) (right panel) driven
 335 trajectories. E. Same as C for β . F. Same as D for β .

336
 337 **CASPT2-levels.** Along the α channel, both XMS-CASPT2, RMS-CASPT2 display,
 338 consistently with the PSB3 study, a further reduced $BLA_{S_1-S_0}$ value and an increase in $E^{90}_{S_1-S_0}$.

339 This points to a further increase in the flatness of the S_1 energy surface that explains the ca. 100 fs
340 τ_{S_1} increase with respect to CASSCF (compare Fig. 4C and 4D) with the RMS-CASPT2
341 trajectories being the slowest and the decay time-range the widest. However, consistently with the
342 CASSCF results, the displayed selectivity favors the -C2=C3- isomerization channel (only at the
343 XMS-CASPT2 level one has a branching to the -C4=C5- channel that, however, has only a 7%
344 QY^{iso}) that displays QY^{iso} values of 0.54 and 0.60 at the XMS-CASPT2 and RMS-CASPT2 levels,
345 respectively and, thus, still close to the PSB3 estimated QY^{iso} . The trajectories calculated with all
346 CAS-level methods for PSB4 are shown in Fig. S8 and Fig. S9.

347 **REKS-levels.** SSR(2,2) and SSR(3,2) share a behavior that is qualitatively different from
348 that described for the CASSCF and the CASPT2-levels. Indeed, slightly larger $E^a_{S_1}$ values as well
349 as very large (20 kcal/mol) $E^{90}_{S_1-S_0}$, point to a much slower dynamics that is demonstrated by the
350 large 64% and 54% fraction of trajectories that do not decay to S_0 within the simulation time when
351 the calculation is performed at the SSR(2,2) and SSR(3,2) levels, respectively. The most dramatic
352 difference displayed is related to the isomerization regioselectivity that strongly favors progression
353 along the alternative -C4=C5- twisting (angle β) rather than along the α angle selected by the
354 wavefunction methods. This is consistent with the differences in the barriers computed along the
355 corresponding S_1 energy profiles that are slightly higher along the -C2=C3- coordinate when
356 computed with the REKS-levels. At the SSR(2,2) level the computed QY^{iso} for -C4=C5-
357 isomerization is very high (0.78). The trajectories calculated with SSR(2,2) and SSR(3,2) for PSB4
358 are shown in Fig. S10 and Fig. S11.

359 We conclude that the dynamics of PSB4 studied at the CASSCF and CASPT2-levels yields
360 the same qualitative mechanisms, timescales and QY^{iso} 's observed in PSB3. However, the
361 corresponding REKS-levels yield a dramatically different dynamics and regioselectivity that are
362 the consequence of a qualitative changes in the electronic structure strongly favoring a COV
363 character of S_1 along the -C2=C3- torsional coordinate α but not along the -C4=C5- coordinate β
364 (see Fig. 4B) as also noticed in previous reports.^{20,51} Again, these changes lead to a change in
365 isomerization regioselectivity, as well as to a change in isomerization timescale.

366 We investigated if the qualitative changes associated with the use of the REKS-levels could
367 be associated with the smaller active space utilized in SSR(2,2) and SSR(3,2) compared to the 8
368 electrons in 8 orbitals of CAS-based methods or to a non-ideal choice of the employed density
369 functional (BHLYP). Moreover, we explore the potential impact of exact exchange on self-

370 interaction error (SIE)⁵² of BHLYP density functional used in SSR calculations. The results of
371 these assessments, that exclusively focused on the reaction paths along α and β , are reported in the
372 last section of the Supporting Information. Briefly, Fig. S12 shows that, as expected, employing
373 XMS-CASPT2 based on a 2 electrons in 2 orbitals active space yields energy profiles more closely
374 resembling the REKS-level, particularly along β , when compared to the XMS-CASPT2 based on
375 8 electrons in 8 orbitals active space. In the same graph we demonstrate the impact of approximate
376 density functional exchange and dynamic electron correlation on the REKS energy profile by
377 comparing BHLYP-REKS and HF-REKS calculations. In fact, switching from the BHLYP-
378 REKS to HF-REKS leads to 50% to 100% increase in the exact electron exchange but to a decrease
379 in dynamic electron correlation (HF-REKS does not account for dynamic electron correlation and
380 is therefore expected to exhibit a behavior more akin to CASSCF(2,2) rather than one of the
381 CASPT2 variants). The results show that HF-REKS yields a better agreement with CASSCF(2,2)
382 and suggest that a functional different from the selected BHLYP may improve the performance
383 of REKS substantially.

384 In order to test this hypothesis we utilized the interface between LIBXC and
385 GAMESS-US⁵³ to compare the S_1 isomerization energy profiles of PSB4 along torsion angle α
386 calculated using SSR-BHLYP(2,2) with 50% of exact exchange; SSR-PBE-2X(2,2) with 54%
387 of exact exchange; and SSR-HFLYP(2,2) with 100% of exact exchange. We demonstrate the
388 results of these calculations in Figure S13, which indicates substantially better agreement between
389 the results of SSR-HFLYP(2,2) and XMS-CASPT2(8,8) calculations than in the case of
390 SSR-BHLYP(2,2). Based on our tests we conclude that the SSR-HFLYP(2,2) method might be
391 a promising option for simulations of PSB models, which is going to be explored further in our
392 future studies.

393

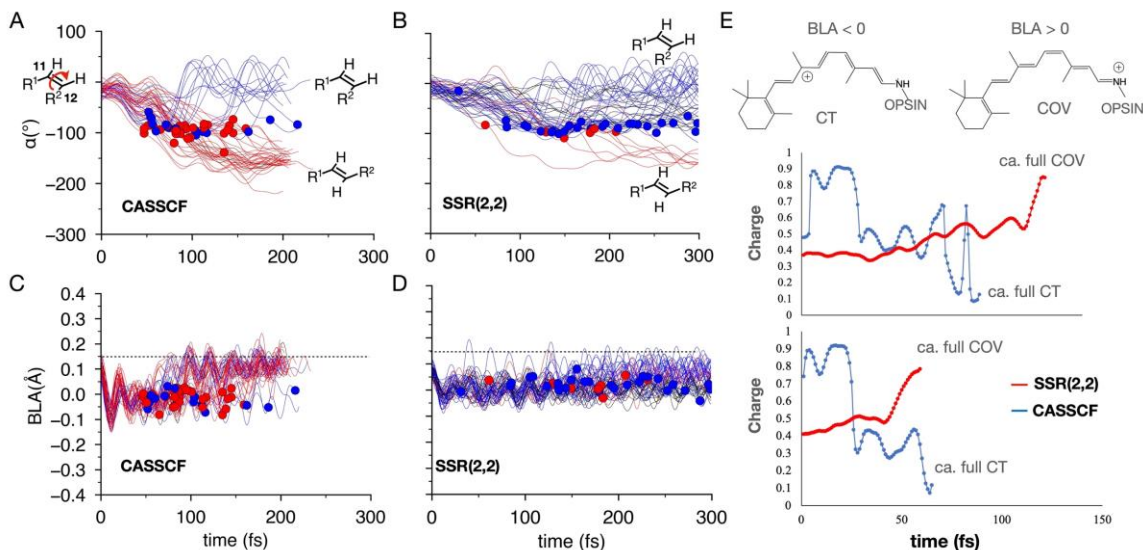
394 **Rh photoisomerization.**

395 We limit our study to CASSCF-driven and SSR(2,2)-driven (“driven” refers to the level of
396 theory used to compute the gradient of the QM-subsystem in Fig. 2B. Of course, also the full QM
397 trajectories discussed above are CASSCF-driven and SSR(2,2)- or SSR(3,2)-driven) QM/MM
398 quantum-classical trajectories (XMS-CASPT2 and RMS-CASPT2 analytical gradient calculations
399 are presently unpractical for the full rPSB chromophore). In the present work, these results are the
400 only one that can be compared with the experimental data in terms of τ_{S1} and QY^{iso} . Consistently

401 with the PSB4 results, we find major differences between calculations carried out using the two
 402 levels of electronic structure theory pointing at substantial discrepancy between CASSCF and the
 403 REKS-levels in systems with longer conjugated chains and, therefore, potentially displaying
 404 multiple isomerization coordinates (i.e. in rPSB the competitive isomerizations would be C9=C10,
 405 C11=C12 and C13=C14). Furthermore, consistently with previous reports,^{5,25} we also find that
 406 only the CASSCF-driven calculations produce results close to the experimental observations.

407 Experimentally the 11-*cis* isomer of rPSB in Rh isomerizes exclusively at the -C11=C12-
 408 bond and in the counterclockwise direction (this is due to the interaction with the chiral protein
 409 cavity). Such a selectivity is reproduced by both the CASSCF-driven and SSR(2,2)-driven
 410 quantum-classical trajectories.^{5,36} In fact, Fig. 5A and 5B show that, at both levels of theory, the
 411 majority of hops have α values (α is now defined by the C10-C11-C12-C13 dihedral) ranging
 412 between -90° and -100° . However, at the CASSCF level, the trajectories hop to S_0 on a 100 fs
 413 decay time-range (from 50 to 150 fs) with no trajectory decaying after 210 fs. In contrast, the
 414 SSR(2,2)-driven decay starts around 100 fs and continues until the end of our simulation. Such a
 415 delay is consistent with previous REKS-driven QM/MM studies of microbial rhodopsins, where
 416 the calculations predicted average S_1 lifetimes 70-80 fs higher than the experimental value in case
 417 of channel rhodopsin and over 100 fs higher in the case of bacteriorhodopsin.^{54,55}

418



419 **Fig. 5.** Propagation of the α along the QM/MM quantum-classical trajectories of bovine rhodopsin. (A)
 420 CASSCF driven trajectories. Red lines and red circles correspond to productive trajectories and their
 421 hopping points, respectively. Blue lines and blue circles correspond to unproductive trajectories and their
 422 hopping points, respectively.

423 hopping points, respectively. Black lines correspond to trajectories that did not undergo surface hop. (B)
424 Same for SSR(2,2) driven trajectories. (C) BLA propagation along the CASSCF driven trajectories. (D)
425 BLA propagation along the SSR(2,2) driven trajectories. (E) CASSCF and SSR(2,2) charge progression
426 along α . The CT weight is inversely proportional to the charge residing on the C12-C13-C14-C15-N
427 moiety.

428
429 The different isomerization progression seen in Fig. 5A and 5B is also reflected in the
430 $BLA_{S_1-S_0}$ values and progression of the BLA coordinate (see Fig. 5C and 5D). The CASSCF and
431 SSR(2,2) levels have $BLA_{S_1-S_0}$ values of 0.12 and 0.06 respectively and therefore similar to the
432 PSB3 and PSB4 values. These descriptors indicate a large change in BLA and therefore a large
433 CT character of the S_1 state at the CASSCF level that changes to a mixed COV/CT character at
434 the SSR(2,2) level (see the corresponding schematic resonance formulas in the top panel of Fig.
435 5E). This is confirmed by the substantial differences in the BLA progression along the CASSCF-
436 driven and SSR(2,2)-driven trajectories. In the first case, one has oscillating S_1 BLA values
437 comprised, roughly, between -0.10 and 0.10 that produce, after decay to S_0 , values comprised
438 between 0.0 and 0.2 typical of a localized S_0 double bonds and pointing to an S_1 state dominated
439 by a CT character. In contrast, SSR(2,2) produces smaller variations in S_1 BLA indicating
440 significantly mixed CT and COV characters that shift to only slightly more positive values after
441 the decay to S_0 . The CASSCF scenario is consistent with the schematic representation of Fig. 2E
442 while the SSR(2,2) description is consistent with the scheme of Fig. 2F. Such an interpretation is
443 supported by plotting the CT evolution (as already done for PSB4 in terms of the charge of a
444 nitrogen containing moiety) along representative CASSCF-driven and SSR(2,2)-driven
445 trajectories (we selected two trajectories that decay at a short timescale (ca. 50 fs, bottom panel in
446 Fig. 5E) and at a longer timescale (ca. 100 fs, middle panel in Fig. 5E). As it can be seen the charge
447 progression is opposite. As previously documented,⁵ the CT character first decreases and then
448 rapidly increases along the CASSCF-driven trajectory explaining the substantial “jump” to more
449 positive values (i.e. towards the COV character) upon decay to S_0 . The opposite is seen along the
450 SSR(2,2)-driven trajectory where the CT weight decreases regularly ultimately favoring a large
451 COV weight. Notice that, in the CASSCF-driven case the initial decrease in CT character (more
452 positive values during the first 25 fs) are explained by a mixing between the S_1 and S_2 being S_2 a
453 diradical state with charge distribution similar, but not identical, to a COV state. Such region is
454 abandoned rapidly.^{5,35,37}

455 The τ_{S1} computed at the SSR(2,2)-driven level reflects a substantially larger distribution of
456 hop points with respect to CASSCF-driven trajectory leading to a much longer τ_{S1} value.
457 Furthermore, and most remarkably, SSR(2,2) produces a strongly reduced QY^{iso} that is only 20%
458 and therefore far from the CASSCF-driven result that is close to the experimental quantity. In
459 conclusion, the QY^{iso} predicted with SSR(2,2) disagree with the established CASSCF and
460 experimental data.^{5,36}

461

462 **III. CONCLUSIONS**

463

464 The presented benchmark study focuses on a specific, but important, class of biomimetic
465 chromophores and shows that the agreement between different levels of electronic structure theory
466 depends on the model employed even when such models are homologue. The comparison between
467 PSB3 and PSB4 is particularly instructive. In PSB3 all levels including CASSCF, the multi-state
468 levels XMS-CASPT2 and RMS-CASPT2 and, remarkably, the REKS levels SSR(2,2) and
469 SSR(3,2) produce the same type of dynamics in terms, for instance, of isomerization timescale and
470 quantum efficiency also including alkyl substituent effects. However, the inclusion of an extra
471 double bond in PSB4 results in a net separation between the CAS-level and the REKS-level. Again,
472 the CASSCF, the multi-state levels XMS-CASPT2 and RMS-CASPT2 display qualitatively
473 similar dynamics. However, the REKS-level produce a qualitatively different dynamics also
474 leading to a change in isomerization regioselectivity. The PSB4 results helps to understand the
475 differences between the presented Rh QM/MM quantum classical trajectory calculations. In fact,
476 while, as indicated by the PSB4 benchmark, the CASSCF-driven and SSR(2,2)-driven calculations
477 produce different dynamics. Furthermore, the wavefunction-based and DFT-based methods yield
478 fundamental differences in the electronic structure (assessed by looking at the charge distribution)
479 of the same retinal chromophore.

480 We find that, in the investigated systems, the QY^{iso} descriptors are relatively insensitive to
481 the details of the S_1 dynamics when comparing CASSCF with the XMS-CASPT2 and RMS-
482 CASPT2 methods (i.e. with and without large dynamic electron correlation) as well as the REKS
483 levels (except for a substantial QY^{iso} increase for the α isomerization seen in PSB4 when using
484 SSR(2,2)). A large difference in QY^{iso} is instead seen when benchmarking the Rh QM/MM model
485 where SSR(2,2) produces a decreased value far from the one experimentally observed.

486 When considering the above observations, one may conclude that the benchmarked REKS
487 variants must be used with care. For instance, they may have limitations when studying the
488 photoisomerization of the retinal chromophore or rPSB models featuring chains with more than
489 three conjugated double bonds. The limitations of SSR(2,2) and SSR(3,2) methods might
490 potentially be associated with their lower ability to describe the change of BLA along the simulated
491 quantum-classical trajectories. Accordingly, it is advisable to test the applicability of SSR(2,2) or
492 SSR(3,2) by comparison with one or more CASPT2-levels methods before running hundreds of
493 trajectories. The comparison must include: 1) the propagation of torsion angle α and BLA along
494 the simulated trajectories, 2) excited state lifetimes, and 3) QY^{iso} along the reactive double bond
495 and, possibly, 4) isomerization regioselectivity. In case of a qualitative agreement, the SSR(2,2)
496 or SSR(3,2) could be applied for extended trajectory studies. Potentially the extension of SSR to
497 SSR(4,4) variant might allow for more universal applicability of REKS. This is a promising
498 research direction that should be addressed in future studies, but it requires additional code
499 development in GAMESS-US since at the moment it only supports SSR(2,2) and SSR(3,2)
500 calculations.

501 In terms of future perspectives, the HF-REKS study of PSB4 mentioned above and detailed
502 in the Supporting Information (Fig. S12) suggests that functionals different from BHLYP may
503 improve the REKS performance through more balanced reductions of the self-interaction error. In
504 fact, our preliminary data (Fig. S13) indicate that SSR(2,2) calculations utilizing HFLYP density
505 functional with 100% of exact exchange demonstrate better agreement with XMS-CASPT2(8,8)
506 calculations than SSR BHLYP(2,2) calculations. Potentially the SIE can be further improved
507 with usage of range-separated hybrid functionals. However, recent publication on SIE
508 demonstrates that range separated functionals do not completely resolve the presence of SIE⁵² and
509 implementation of REKS calculations in connection with range-separated hybrid functionals in
510 GAMESS-US would require further code development.

511 Finally, based on recent publications^{56,57}, an enhancement of REKS performance might be
512 attained by re-formulating REKS within the framework of the density-corrected DFT method (DC-
513 DFT). In fact, for many heteronuclear molecules, the DC-DFT method has shown an accuracy
514 increase in generating PESs with respect to semilocal DFT⁵⁷. Thus, combining DC-DFT with
515 REKS may offer an avenue to improve the ability of REKS in describing the PESs of rPSB models
516 in general.

517

518 **IV. METHODS**

519

520 All calculations were performed with 6-31G* basis set. OpenMolcas and
521 OpenMolcas/Tinker^{34,58,59} were used for all CASPT2-levels QM and QM/MM calculations,
522 respectively. The OpenMolcas-GAMESS-US/Tinker interface^{34,60-62} was used for all REKS
523 calculations. The complete active spaces (CAS) were defined as following for each system:
524 CAS(6,6) for PSB3 and substituted PSB3 models, CAS(8,8) for PSB4 model, CAS(12,12) for full
525 retinal model in bovine rhodopsin namely, all the π and π^* orbitals associated to the conjugated
526 polyenic chains. In addition we used CAS(2,2) active space alongside with CAS(8,8) in XMS-
527 CASPT2 calculations of potential energy scans in PSB4 model to elucidate the effect of reduced
528 active space in REKS methods. All REKS calculations and calculations based on CAS(2,2) include
529 only the HOMO and LUMO, π and π^* orbitals in the active space. REKS calculations in present
530 work are done with BHLYP functional.⁴⁷⁻⁴⁹

531

532 **Construction of the S1 potential energy scans in PSB models**

533 The potential energy scans are constructed by constraining the geometries of PSB models at values
534 of torsion angle α ranging between 0 and 90 degrees (using increment of 2 degrees) with
535 subsequent geometry optimization of the given structure in S₁ electronic state. In Fig.s representing
536 the potential energy scans we report the S₁ and S₀ energies corresponding to these structures. In
537 case of PSB4 model we calculate the isomerization energy profiles along both torsion angle α and
538 torsion angle β . The potential energy scan for each of the PSB models was done at CASSCF,
539 XMS-CASPT2, RMS-CASPT2, SSR(2,2), and SSR(3,2) levels of theory.

540

541 **Quantum-Classical trajectory computations in PSB models**

542 The initial conditions are generated using Wigner sampling where the vibrational frequencies are
543 calculated using the corresponding CAS-based or REKS method. The propagation of trajectories
544 is quantum-classical where the surface hopping is treated with Tully's fewest switches⁶³, along
545 with the Hammes-Schiffer/Tully scheme⁶⁴ and the decoherence correction by Granucci and
546 Persico,⁶⁵ while the hopping criteria is based on hopping probability. The excited state trajectories
547 are initiated in Franck-Condon region and initially executed for 300 fs; if over 10% of trajectories

548 remains on the excited state potential energy surface, the simulations are extended until the total
549 simulation time reaches 600 fs. The molecular dynamics for each of the PSB models was done at
550 CASSCF, XMS-CASPT2, RMS-CASPT2, SSR(2,2), and SSR(3,2) levels of theory. For each
551 method we used 50 trajectories.

552

553 **Rh QM/MM model preparation**

554 The Rh QM/MM model was constructed starting from the 2.2 Å resolution crystallographic
555 structure available in the Protein Data Bank (PDB ID 1U19)⁶⁶ using the methodology described in
556 our previous publications.^{5,36} To generate 50 initial conditions constituent of starting geometries
557 and velocities using Boltzmann distribution corresponding to room temperature we utilized the
558 following protocol:

559 1) A 20 ns room-temperature dynamics simulation was performed at MM level starting from the
560 S₀ equilibrium structure of the Rh QM/MM model with GROMACS.⁶⁷ The MD relaxations consist
561 of a 50 ps heating followed by 150 ps room-temperature equilibration and 20 ns production with
562 a time interval of 1 fs. The input velocities are generated according to a Maxwell distribution at
563 temperature of 298 K with a random seed and using the Berendsen thermostat.

564 2) Along the MM dynamics, 200 snapshots (geometries and velocities) were extracted from the 20
565 ns production MD at every 100 ps time interval. In present benchmark paper we only utilize 50 of
566 these snapshots.

567 3) Each snapshot was then employed to start a HF/6-31G*/Amber level 200 fs trajectory followed
568 by a 50 fs a 2-root-state-average CASSCF/6-31G*/Amber level of theory on the S₀ PES with time
569 step of 1 fs. In case of SSR(2,2) simulations we perform the ground state equilibration using 200
570 fs trajectory with SSR(2,2)-REKS/6-31G*/Amber level of theory.

571 The geometries and velocities of the final (last time step) form the set representing the Boltzmann
572 distribution and, therefore, the initial conditions for S₁ population dynamics.

573

574 **Supporting Information**

575 Exponential fit of S₁ life-time for each model system. Steric repulsion estimate. The complete
576 isomerization energy profiles along the -C2=C3- isomerization coordinate (α) in 1cMePSB3,
577 4cMePSB3, and 4tMePSB3. PSB3, 1cMePSB3, 4cMePSB3, and 4tMePSB3 trajectories produced
578 by CASPT2-levels. PSB3, 1cMePSB3, 4cMePSB3, and 4tMePSB3 trajectories produced by
579 REKS methods. PSB4 trajectories produced by CASPT2-levels. PSB4 trajectories produced by

580 REKS methods. Effect of reduced active space and percentage of exact exchange on the S₁
581 isomerization energy profiles of PSB4.

582

583 Acknowledgements

584 M. O. and D. K. acknowledges support from NSF CSDM-A Grant No. 2102619. M.O. is also
585 grateful for a European-Union, Next Generation EU, MIUR Italia Domani Progetto mRNA Spoke 6
586 del “National Center for Gene Therapy and Drugs based on RNA Technology”. – CUP
587 B63C22000610006. N. F. and M.H.-R. acknowledge the financial support by Agence Nationale de la
588 Recherche (project ULTRArchea, grant ANR-21-CE11-0029-03).

589

590 Reference

- 591 (1) Garavelli, M.; Celani, P.; Bernardi, F.; Robb, M. A.; Olivucci, M. The C₅H₆NH₂⁺
592 Protonated Schiff Base: An Ab Initio Minimal Model for Retinal Photoisomerization. *J.*
593 *Am. Chem. Soc.* **1997**, *119*, 6891–6901.
- 594 (2) Vreven, T.; Bernardi, F.; Garavelli, M.; Olivucci, M.; Robb, M. A.; Schlegel, H. B. Ab
595 Initio Photoisomerization Dynamics of a Simple Retinal Chromophore Model. *J. Am.*
596 *Chem. Soc.* **1997**, *119*, 12687–12688.
- 597 (3) Weingart, O.; Migani, A.; Olivucci, M.; Robb, M. A.; Buss, V.; Hunt, P. Probing the
598 Photochemical Funnel of a Retinal Chromophore Model via Zero-Point Energy Sampling
599 Semiclassical Dynamics. *J. Phys. Chem. A* **2004**, *108*, 4685–4693.
- 600 (4) Barbatti, M.; Ruckebauer, M.; Szymczak, J. J.; Aquino, A. J. A.; Lischka, H.
601 Nonadiabatic Excited-State Dynamics of Polar π -Systems and Related Model Compounds
602 of Biological Relevance. *Phys. Chem. Chem. Phys.* **2008**, *10*, 482–494.
- 603 (5) Xuchun Yang; Madushanka Manathunga; Gozem, S.; Léonard, J.; Andruniów, T.;
604 Olivucci, M. Quantum–Classical Simulations of Rhodopsin Reveal Excited-State
605 Population Splitting and Its Effects on Quantum Efficiency. *Nat. Chem.* **2022**, *14*, 441–
606 449.
- 607 (6) Rivalta, I.; Nenov, A.; Garavelli, M. Modelling Retinal Chromophores
608 Photoisomerization: From Minimal Models in Vacuo to Ultimate Bidimensional
609 Spectroscopy in Rhodopsins. *Phys. Chem. Chem. Phys.* **2014**, *16*, 16865–16879.
- 610 (7) Gozem, S.; Melaccio, F.; Lindh, R.; Krylov, A. I.; Granovsky, A. A.; Angeli, C.; Olivucci,
611 M. Mapping the Excited State Potential Energy Surface of a Retinal Chromophore Model
612 with Multireference and Equation-of-Motion Coupled-Cluster Methods. **2013**.
- 613 (8) Gozem, S.; Krylov, A. I.; Olivucci, M. Conical Intersection and Potential Energy Surface
614 Features of a Model Retinal Chromophore: Comparison of EOM-CC and Multireference
615 Methods. *J. Chem. Theory Comput.* **2013**, *9*, 284–292.
- 616 (9) Tuna, D.; Lefrancois, D.; Wolański, Ł.; Gozem, S.; Schapiro, I.; Andruniów, T.; Dreuw,
617 A.; Olivucci, M. Assessment of Approximate Coupled-Cluster and Algebraic-
618 Diagrammatic-Construction Methods for Ground- and Excited-State Reaction Paths and
619 the Conical-Intersection Seam of a Retinal-Chromophore Model. *J. Chem. Theory*
620 *Comput.* **2015**, *11*, 5758–5781.
- 621 (10) Gozem, S.; Huntress, M.; Schapiro, I.; Lindh, R.; Granovsky, A. A.; Angeli, C.; Olivucci,
622 M. Dynamic Electron Correlation Effects on the Ground State Potential Energy Surface of
623 a Retinal Chromophore Model. *J. Chem. Theory Comput.* **2012**, *8*, 4069–4080.
- 624 (11) Zen, A.; Coccia, E.; Gozem, S.; Olivucci, M.; Guidoni, L. Quantum Monte Carlo
625 Treatment of the Charge Transfer and Diradical Electronic Character in a Retinal

- 626 Chromophore Minimal Model. *J. Chem. Theory Comput.* **2015**, *11*, 992–1005.
- 627 (12) Cembran, A.; González-Luque, R.; Serrano-Andrés, L.; Merchán, M.; Garavelli, M. About
628 the Intrinsic Photochemical Properties of the 11-Cis Retinal Chromophore: Computational
629 Clues for a Trap State and a Lever Effect in Rhodopsin Catalysis. *Theor. Chem. Acc.*
630 **2007**, *118*, 173–183.
- 631 (13) Gozem, S.; Melaccio, F.; Valentini, A.; Filatov, M.; Huix-Rotllant, M.; Ferré, N.; Frutos,
632 L. M.; Angeli, C.; Krylov, A. I.; Granovsky, A. A.; et al. Shape of Multireference,
633 Equation-of-Motion Coupled-Cluster, and Density Functional Theory Potential Energy
634 Surfaces at a Conical Intersection. *J. Chem. Theory Comput.* **2014**, *10*, 3074–3084.
- 635 (14) Park, J. W. Single-State Single-Reference and Multistate Multireference Zeroth-Order
636 Hamiltonians in MS-CASPT2 and Conical Intersections. *J. Chem. Theory Comput.* **2019**,
637 *15*, 3960–3973.
- 638 (15) Zhang, X.; Herbert, J. M. Nonadiabatic Dynamics with Spin-Flip vs Linear-Response
639 Time-Dependent Density Functional Theory: A Case Study for the Protonated Schiff Base
640 C5H6NH⁺. *J. Chem. Phys.* **2021**, *155*.
- 641 (16) Filatov, M.; Min, S. K.; Kim, K. S. Direct Nonadiabatic Dynamics by Mixed Quantum-
642 Classical Formalism Connected with Ensemble Density Functional Theory Method:
643 Application to Trans-Penta-2,4-Dieniminium Cation. *J. Chem. Theory Comput.* **2018**, *14*,
644 4499–4512.
- 645 (17) Liu, L.; Liu, J.; Martinez, T. J. Dynamical Correlation Effects on Photoisomerization: Ab
646 Initio Multiple Spawning Dynamics with MS-CASPT2 for a Model Trans-Protonated
647 Schiff Base. *J. Phys. Chem. B* **2016**, *120*, 1940–1949.
- 648 (18) Huix-Rotllant, M.; Filatov, M.; Gozem, S.; Schapiro, I.; Olivucci, M.; Ferré, N.
649 Assessment of Density Functional Theory for Describing the Correlation Effects on the
650 Ground and Excited State Potential Energy Surfaces of a Retinal Chromophore Model. *J.*
651 *Chem. Theory Comput.* **2013**, *9*, 3917–3932.
- 652 (19) Valsson, O.; Filippi, C.; Casida, M. E. Regarding the Use and Misuse of Retinal
653 Protonated Schiff Base Photochemistry as a Test Case for Time-Dependent Density-
654 Functional Theory. *J. Chem. Phys.* **2015**, *142*.
- 655 (20) Bin, X.; Momen, R.; Xu, T.; Kirk, S. R.; Filatov, M.; Jenkins, S. A 3-D Bonding
656 Perspective of the Factors Influencing the Relative Stability of the S₁/S₀ Conical
657 Intersections of the Penta-2,4-Dieniminium Cation (PSB3). *Int. J. Quantum Chem.* **2019**,
658 *119*, 1–11.
- 659 (21) Liu, F.; Filatov, M.; Martínez, T. J. Analytical Derivatives of the Individual State Energies
660 in Ensemble Density Functional Theory. II. Implementation on Graphical Processing
661 Units (GPUs). *J. Chem. Phys.* **2021**, *154*.
- 662 (22) Szefczyk, B.; Grabarek, D.; Walczak, E.; Andruniów, T. Excited-State Minima and
663 Emission Energies of Retinal Chromophore Analogues: Performance of CASSCF and
664 CC2 Methods as Compared with CASPT2. *J. Comput. Chem.* **2017**, *38*, 1799–1810.
- 665 (23) Sen, S.; Schapiro, I. A Comprehensive Benchmark of the XMS-CASPT2 Method for the
666 Photochemistry of a Retinal Chromophore Model. *Mol. Phys.* **2018**, *116*, 2571–2582.
- 667 (24) Valsson, O.; Filippi, C. Photoisomerization of Model Retinal Chromophores: Insight from
668 Quantum Monte Carlo and Multiconfigurational Perturbation Theory. *J. Chem. Theory*
669 *Comput.* **2010**, *6*, 1275–1292.
- 670 (25) Manathunga, M.; Yang, X.; Luk, H. L.; Gozem, S.; Frutos, L. M.; Valentini, A.; Ferrè, N.;
671 Olivucci, M. Probing the Photodynamics of Rhodopsins with Reduced Retinal

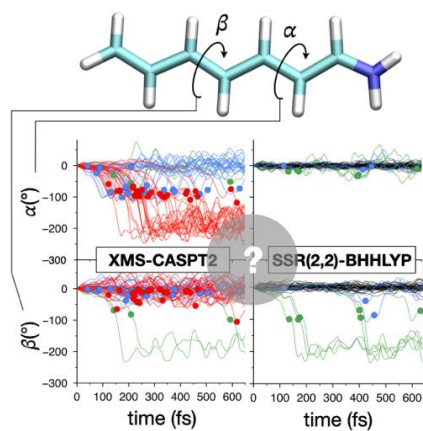
- 672 Chromophores. *J. Chem. Theory Comput.* **2016**, *12*, 839–850.
- 673 (26) Shiozaki, T.; Gyroffy, W.; Celani, P.; Werner, H. J. Communication: Extended Multi-
674 State Complete Active Space Second-Order Perturbation Theory: Energy and Nuclear
675 Gradients. *J. Chem. Phys.* **2011**, *135*.
- 676 (27) Nishimoto, Y.; Battaglia, S.; Lindh, R. Analytic First-Order Derivatives of (X)MS, XDW,
677 and RMS Variants of the CASPT2 and RASPT2 Methods. *J. Chem. Theory Comput.*
678 **2022**, *18*, 4269–4281.
- 679 (28) Battaglia, S.; Lindh, R. On the Role of Symmetry in XDW-CASPT2. *J. Chem. Phys.*
680 **2021**, *154*.
- 681 (29) Filatov, M. Spin-Restricted Ensemble-Referenced Kohn-Sham Method: Basic Principles
682 and Application to Strongly Correlated Ground and Excited States of Molecules. *Wiley*
683 *Interdiscip. Rev. Comput. Mol. Sci.* **2015**, *5*, 146–167.
- 684 (30) Lee, S.; Park, W.; Nakata, H.; Filatov, M.; Choi, C. H. Recent Advances in Ensemble
685 Density Functional Theory and Linear Response Theory for Strong Correlation. *Bull.*
686 *Korean Chem. Soc.* **2022**, *43*, 17–34.
- 687 (31) Filatov, M.; Lee, S.; Choi, C. H. Description of Sudden Polarization in the Excited
688 Electronic States with an Ensemble Density Functional Theory Method. *J. Chem. Theory*
689 *Comput.* **2021**, *17*, 5123–5139.
- 690 (32) Filatov(Gulak), M.; Paolino, M.; Pierron, R.; Cappelli, A.; Giorgi, G.; Léonard, J.; Huix-
691 rotllant, M.; Ferré, N.; Yang, X.; Kaliakin, D.; et al. Towards the Engineering of a Photon-
692 Only Two-Stroke Rotary Molecular Motor. *Nat. Commun.* **2022**, *13*, 6433.
- 693 (33) Kaliakin, D. S. OpenMolcas–GAMESS/Tinker Interface Repository.
- 694 (34) Manni, G. L.; Galván, I. F.; Alavi, A.; Aquilante, F.; Autschbach, J.; Baiardi, A.; Bao, J.
695 J.; Battaglia, S.; Blanco-gonzález, A.; Bokarev, S. I.; et al. The OpenMolcas Web : A
696 Community-Driven Approach to Advancing Computational Chemistry. *J. Chem. Theory*
697 *Comput.* **2023**, 1–126.
- 698 (35) Manathunga, M.; Yang, X.; Orozco-Gonzalez, Y.; Olivucci, M. Impact of Electronic State
699 Mixing on the Photoisomerization Time Scale of the Retinal Chromophore. *J. Phys.*
700 *Chem. Lett.* **2017**, *8*, 5222–5227.
- 701 (36) Schnedermann, C.; Yang, X.; Liebel, M.; Spillane, K.; Lugtenburg, J.; Fernandez, I.;
702 Valentini, A.; Schapiro, I.; Olivucci, M.; Kukura, P. Evidence for a Vibrational Phase-
703 Dependent Isotope Effect on the Photochemistry of Vision. *Nat. Chem.* **2018**, *10*, 449–
704 455.
- 705 (37) Manathunga, M.; Yang, X.; Olivucci, M. Electronic State Mixing Controls the
706 Photoreactivity of a Rhodopsin with All- Trans Chromophore Analogues. *J. Phys. Chem.*
707 *Lett.* **2018**, *9*, 6350–6355.
- 708 (38) Szymczak, J. J.; Barbatti, M.; Lischka, H. Is the Photoinduced Isomerization in Retinal
709 Protonated Schiff Bases a Single- or Double-Torsional Process. *J. Phys. Chem. A* **2009**,
710 *113*, 11907–11918.
- 711 (39) Roos, B. O.; Taylor, P. A Complete Active Space SCF Method (CASSCF) Using a
712 Density Matrix Formulated Super-CI Approach. *Chem. Phys.* **1980**, *48*, 157–173.
- 713 (40) Roos, B. O. Multiconfigurational Quantum Chemistry for Ground and Excited States. In
714 *Radiation Induced Molecular Phenomena in Nucleic Acids: A Comprehensive Theoretical*
715 *and Experimental Analysis*; Shukla, M. K.; Leszczynski, J., Eds.; Springer Netherlands:
716 Dordrecht, 2008; pp. 125–156.
- 717 (41) Marín, M. D. C.; De Vico, L.; Dong, S. S.; Gagliardi, L.; Truhlar, D. G.; Olivucci, M.

- 718 Assessment of MC-PDFT Excitation Energies for a Set of QM/MM Models of
719 Rhodopsins. *J. Chem. Theory Comput.* **2019**, *15*, 1915–1923.
- 720 (42) Park, J. W.; Shiozaki, T. Analytical Derivative Coupling for Multistate CASPT2 Theory.
721 *J. Chem. Theory Comput.* **2017**, *13*, 2561–2570.
- 722 (43) Oliveira, L. N.; Gross, E. K. U.; Kohn, W. Ensemble-Density Functional Theory. *Int. J.*
723 *Quantum Chem. Quantum Chem. Symp.* **1990**, *24*, 707–716.
- 724 (44) Ferre, N.; Filatov, M.; Huix-Rotllant, M. Density-Functional Methods for Excited States.
725 *Top. Curr. Chem.* **2016**, *368*, 97–124.
- 726 (45) Filatov, M. Assessment of Density Functional Methods for Obtaining Geometries at
727 Conical Intersections in Organic Molecules. *J. Chem. Theory Comput.* **2013**, *9*, 4526–
728 4541.
- 729 (46) Mai, S.; González, L. Molecular Photochemistry: Recent Developments in Theory.
730 *Angew. Chemie - Int. Ed.* **2020**, *59*, 16832–16846.
- 731 (47) Becke, A. D. Density-Functional Exchange-Energy Approximation with Correct
732 Asymptotic Behavior. *Phys. Rev. A* **1988**, *38*, 3098–3100.
- 733 (48) Lee, C.; Hill, C.; Carolina, N. Development of the Colle-Salvetti Correlation-Energy
734 Formula into a Functional of the Electron Density. *Phys. Rev. A* **1988**, *37*, 785–789.
- 735 (49) Becke, A. D. A New Mixing of Hartree-Fock and Local Density-Functional Theories. *J.*
736 *Chem. Phys.* **1993**, *98*, 1372–1377.
- 737 (50) Chatterjee, G.; Jha, A.; Blanco-Gonzalez, A.; Tiwari, V.; Manathunga, M.; Duan, H. G.;
738 Tellkamp, F.; Prokhorenko, V. I.; Ferré, N.; Dasgupta, J.; et al. Torsionally Broken
739 Symmetry Assists Infrared Excitation of Biomimetic Charge-Coupled Nuclear Motions in
740 the Electronic Ground State. *Chem. Sci.* **2022**, *13*, 9392–9400.
- 741 (51) Ping, Y.; Xu, T.; Momen, R.; Azizi, A.; Kirk, S. R.; Filatov, M.; Jenkins, S. Isomerization
742 of the RPSB Chromophore in the Gas Phase along the Torsional Pathways Using QTAIM.
743 *Chem. Phys. Lett.* **2017**, *685*, 222–228.
- 744 (52) Lonsdale, D. R.; Goerigk, L. One-Electron Self-Interaction Error and Its Relationship to
745 Geometry and Higher Orbital Occupation. *J. Chem. Phys.* **2023**, *158*.
- 746 (53) Gerasimov, I. S.; Zahariev, F.; Leang, S. S.; Tesliuk, A.; Gordon, M. S.; Medvedev, M. G.
747 Introducing LibXC into GAMESS (US). *Mendeleev Commun.* **2021**, *31*, 302–305.
- 748 (54) Liang, R.; Liu, F.; Martínez, T. J. Nonadiabatic Photodynamics of Retinal Protonated
749 Schiff Base in Channelrhodopsin 2. *J. Phys. Chem. Lett.* **2019**, 2862–2868.
- 750 (55) Yu, J. K.; Liang, R.; Liu, F.; Martínez, T. J. First-Principles Characterization of the
751 Elusive i Fluorescent State and the Structural Evolution of Retinal Protonated Schiff Base
752 in Bacteriorhodopsin. *J. Am. Chem. Soc.* **2019**, *141*, 18193–18203.
- 753 (56) Wasserman, A.; Nafziger, J.; Jiang, K.; Kim, M. C.; Sim, E.; Burke, K. The Importance of
754 Being Inconsistent. *Annu. Rev. Phys. Chem.* **2017**, *68*, 555–581.
- 755 (57) Kim, M.-C.; Park, H.; Son, S.; Sim, E.; Burke, K. Improved DFT Potential Energy
756 Surfaces via Improved Densities. *J. Phys. Chem. Lett.* **2015**, *6*, 3802–3807.
- 757 (58) Fdez. Galván, I.; Vacher, M.; Alavi, A.; Angeli, C.; Aquilante, F.; Autschbach, J.; Bao, J.
758 J.; Bokarev, S. I.; Bogdanov, N. A.; Carlson, R. K.; et al. OpenMolcas: From Source Code
759 to Insight. *J. Chem. Theory Comput.* **2019**, *15*, 5925–5964.
- 760 (59) Ponder, J. W.; Richards, F. M. Tinker Molecular Modeling Package. *J. Comput. Chem.*
761 **1987**, *8*, 1016–1024.
- 762 (60) Huix-Rotllant, M.; Ferré, N. Analytic Energy, Gradient, and Hessian of Electrostatic
763 Embedding QM/MM Based on Electrostatic Potential-Fitted Atomic Charges Scaling

- 764 Linearly with the MM Subsystem Size. *J. Chem. Theory Comput.* **2021**, *17*, 538–548.
- 765 (61) Gordon, M. S.; Schmidt, M. W. Advances in Electronic Structure Theory: GAMESS a
766 Decade Later. In *Theory and Applications of Computational Chemistry*; Dykstra C.E.;
767 Frenking G.; Kim K.S.; Scuseria G.E., Eds.; Elsevier: Amsterdam, 2005; pp. 1167–1189.
- 768 (62) Schmidt, M. W.; Baldridge, K. K.; Boatz, J. A.; Elbert, S. T.; Gordon, M. S.; Jensen, J. H.;
769 Koseki, S.; Matsunaga, N.; Nguyen, K. A.; Su, S. J. et al. General Atomic and Molecular
770 Electronic Structure System. *J. Comput. Chem.* **1993**, *14*, 1347–1363.
- 771 (63) Tully, J. C. Molecular Dynamics with Electronic Transitions. *J. Chem. Phys.* **1990**, *93*,
772 1061–1071.
- 773 (64) Hammes-Schiffer, S.; Tully, J. C. Proton Transfer in Solution: Molecular Dynamics with
774 Quantum Transitions. *J. Chem. Phys.* **1994**, *101*, 4657–4667.
- 775 (65) Granucci, G.; Persico, M. Critical Appraisal of the Fewest Switches Algorithm for Surface
776 Hopping. *J. Chem. Phys.* **2007**, *126*.
- 777 (66) Okada, T.; Sugihara, M.; Bondar, A.-N.; Elstner, M.; Entel, P.; Buss, V. The Retinal
778 Conformation and Its Environment in Rhodopsin in Light of a New 2.2Å Crystal
779 Structure. *J. Mol. Biol.* **2004**, *342*, 571–583.
- 780 (67) Pronk, S.; Páll, S.; Schulz, R.; Larsson, P.; Bjelkmar, P.; Apostolov, R.; Shirts, M. R.;
781 Smith, J. C.; Kasson, P. M.; Van Der Spoel, D.; et al. GROMACS 4.5: A High-
782 Throughput and Highly Parallel Open Source Molecular Simulation Toolkit.
783 *Bioinformatics* **2013**, *29*, 845–854.
- 784
- 785

786
787

TOC



788